Far Ultraviolet carbon emissions in the Mars aurora: Brightness, intensity ratios and seasonal dependence

J.C. Gérard, L. Soret, B. Hubert
LPAP, STAR Institute, Université de Liège, Liège, Belgium

R. Lillis, SSL, University of California, Berkeley, USA

S. Jain, J. Deighan, LASP, University of Colorado, Boulder, USA

Published in ICARUS, 448, 116919 (2026)
doi 10.1016/j.icarus.2025.116919

Corresponding author

Jean-Claude Gérard

Postal address:
Laboratoire de Physique Atmosphérique et Planétaire
STAR Institute
Université de Liège – B5c
Allée du 6 août, 19c
4000-Liège (Belgium)

e-mail: jc.gerard@uliege.be
Phone : +32-479874895

HIGHLIGHS

- Monte Carlo simulations of the brightness of the carbon auroral emissions at 156.1 and 165.7 nm
- Production dominated by dissociative excitation of CO_2 resulting in no significant multiple scattering
- Intensity ratios between the OI 130.4, 135.6 nm and the CI 156.1 nm, 165.7 nm emissions depend on auroral electron energy
- Simulation results compare well with EMM/EMUS spectrometer observations

ABSTRACT

Neutral carbon emissions have been observed in Far Ultraviolet spectra (FUV) of the Martian aurora with the Emirates Mars Ultraviolet Spectrometer (EMUS) instrument on board the Emirates Mars Mission (EMM). Oxygen emissions at 130.4 and 135.6 nm have been used to map the auroral morphology and its dependence on solar wind parameters. The CI emissions at 156.1 and 165.7 nm are excited by collisions between energetic electrons and CO_2, CO and C. We present Monte Carlo simulations of the altitude distributions of both features showing that electron collisions with ambient CO_2 molecules are the dominant source, followed by collisions on CO, while direct impact on C atoms is several orders of magnitude smaller. Since the C atom fragments resulting from dissociation are produced with a speed exceeding by far the thermal velocity, the optical depth is negligible. Consequently, the 156.1 and 165.7 nm photons are not self-absorbed, and the calculation of the emission rates does not require consideration of radiative transfer, unlike the OI 130.4 nm triplet. We present calculations of the efficiency of the carbon emissions for a range of incident auroral electrons energies. We illustrate the energy dependence of the intensity ratios between the oxygen 130.4 and 135.6 nm and the carbon 165.7 nm emissions. These ratios may be used to remotely characterize the spatial distribution of the incident electron energies in spectral FUV maps of the aurora.

KEYWORDS

Planetary atmospheres (1244)
Mars (1007)
Aurorae
Atomic spectroscopy (2099)
Line intensities (2084)

1. INTRODUCTION

Carbon dayglow emissions in the Martian upper atmosphere were first observed by Barth et al. (1971) with the ultraviolet spectrometer during the Mariner 6 and 7 flybys They detected the presence of several CI emissions, including a clear identification of the 156.1 and 165.7 nm multiplets. The 165.7 nm emission reached a peak of 1.7 kilorayleigh (1 kR = 10^9 photons cm^{-2} s^{-1} emitted in 4π steradians). They deduced that the main source of excitation was photodissociative excitation or photoelectron dissociative excitation of CO_2 with a possible contribution of resonance scattering of C atoms, as later confirmed with the model calculations by Fox and Dalgarno (1979). This identification was confirmed by Feldman et al. (2000) who observed the dayside disk spectrum of Mars with the ASTRO-2 observatory on board the Space Shuttle Endeavour. In these dayglow spectra, the brightest feature in the spectral range 132 – 170 nm was the CI multiplet at 165.7 nm. Its presence was also reported in spectra observed with the SPICAM instrument on board the Mars Express orbiter by Leblanc et al. (2006a) and in the data collected with the Emirates Mars Ultraviolet Spectrometer (EMUS) spectrometer (Holsclaw et al., 2021) on board the Emirates Mars Mission (EMM) by Jain et al. (2022). A detailed study of the 156.1 and 165.7 nm Mars dayglow was performed by Lo et al. (2022) based on extensive vertical, latitudinal and seasonal measurements of the limb brightness of this emission from the Imaging UltraViolet Spectrometer (IUVS) on the Mars Atmosphere and Volatile EvolutioN (MAVEN) orbiter. They found that dissociation of CO_2 by photoelectron impact is the major production below about 155 km while resonance scattering of C atoms dominates at higher altitudes. Both dayglow emissions have also been observed on Venus with PV-OUVS on Pioneer Venus (Paxton, 1985), HUT (Feldman et al., 2000) and during the Cassini flyby of Venus (Hubert et al., 2010, 2012). Similarly to Mars, it was found that electron impact and photodissociation of CO_2 are dominant sources together with resonance scattering of carbon atoms.

Observations of these carbon emissions in the Mars aurora have been scarce so far. Bertaux et al. (2005) and Leblanc et al. (2006b) identified their marginal presence in SPICAM nightside spectra. It was confirmed in the spectra collected with EMUS by Lillis et al. (2022). The nadir brightness was on the order of 1 Rayleigh/nm. Observations of the OI resonance 3s $^3S^0 \rightarrow 2p^4\ ^3P$ triplet at 130.4 nm serves as the basis of the EMUS auroral morphological studies. The EMUS global observations show that the FUV aurora is more widespread than initially observed with less sensitive instruments. They show a high occurrence frequency in regions void of crustal magnetic field such as the northern hemisphere and regions of open magnetic topology (Chirakkil et al., 2024). Aurora events also tend to occur more frequently near the terminator and show a seasonal dependence. Lillis et al. (2022) described a new type of aurora exhibiting a sinuous structure stretching thousands of kilometers from near midnight into the nightside in the northern hemisphere. It appears to be linked to electron energization in the magnetotail current sheet (Lillis et al., 2024).

However, the transition giving rise to this emission is optically thick in most observing conditions (Soret et al., 2024) so that its observed nadir or limb brightness does not provide a direct estimate of the O (^{3}S) production rate and necessitates the use of detailed radiative transfer calculations. The excitation cross sections of the carbon lines by electron impact on CO_2, CO and C atoms are reasonably well known. In contrast to the oxygen resonance multiplet, the two carbon transitions are optically thin, given the low carbon atom abundance in the Martian upper atmosphere. Consequently, the study of the 156.1 nm and 165.7 nm carbon emissions provides a more straightforward access to the excitation rate and thus to the rate of collisional impact by auroral electrons.

In this study, we investigate the relation between the auroral electron energy and the production of the two FUV carbon features. We examine the expected nadir brightness as a function of the energy of the precipitating electrons. We also use numerical Monte Carlo simulations to determine how the ratio of the carbon emissions to the OI 130.4 nm may be used to determine the characteristic energy of the electron precipitation.

In section 2, we describe the spectral components and sources of the excited C atoms in the nightside aurora, the relevant cross sections and the Monte Carlo simulations. Results of Monte Carlo simulations are described and commented in section 3. Section 4 discusses the combination of the 130.4 and 135.6 nm oxygen and carbon emissions as indicators of the electron characteristic energy. The predicted ratios are compared with statistical EMM/EMUS measurements of the FUV OI and CI line brightness in section 5.

2. Model of the carbon line emissions

2.1 Sources

The FUV 165.7 nm and 156.1 nm multiplets correspond to the CI $2s^22p3s\ ^3P^0 \rightarrow 2s^22p^2\ ^3P$ and $2s^2p^3\ ^3D^o \rightarrow 2s^22p^2\ ^3P$ resonance transitions respectively. In the nightside aurora, they are produced by electron collisions with carbon dioxide, carbon monoxide and carbon atoms:

dissociative excitation of CO_2 and CO:

$$CO_2 + e\ (E > 24.1\ eV, 24.5\ eV) \rightarrow C(^3P^0, ^3D^0) + 2O + e \qquad (1)$$

$$CO + e(E > 18.6\ eV, 19.1\ eV) \rightarrow C(^3P^0, ^3D^0\ ) + O + e \qquad (2)$$

direct collisional excitation of C atoms:

$$C + e(E > 7.48\ eV) \rightarrow C(^3D^0) + e \qquad (3)$$

$$C + e(E > 7.95\ eV) \rightarrow C(^3P^0) + e \qquad (4)$$

For the energy dependence of the excitation cross section (1), we use the laboratory measurements by Mumma et al. (1972) between threshold and 300 eV revised by Ajello et al. (2019) to account for the re-measurement of the HI Lyman-α reference cross section (Itikawa, 2002). The values at 100 eV are 4.3×10^{-19} cm^2 at 156.1 nm and 8.3×10^{-19} cm^2 at 165.7 nm. The uncertainty was estimated to be ±30%. They have been extrapolated to higher energies using a Born approximation.

For the cross section of process (2), following Lo et al. (2021), we use the analytical expression by Green and Barth (1965):

$$\sigma(E) = \frac{q_0 F}{W^2}\ (1 - \frac{W}{E})^{\beta}\ (\frac{W}{E})^{\Omega},$$

where E is the kinetic energy of the incident electrons, W the threshold energy of the process in eV and parameters q_0, F, β and Ω are taken from the analytical fit by Lo et al. (2021). It is normalized to the laboratory measurements at 30 and 100 eV by Ajello et al. (2019) with the correction made by Lo et al. (2021), giving values of 1.77×10^{-18} cm^2 for 156.1 nm and 1.62×10^{-18} cm^2 for 165.7 nm at 100 eV.

For direct excitation of carbon atoms (3) we adopt the excitation cross sections calculated by Wang et al. (2013) between threshold and 60 eV. They are significantly lower than earlier values by Dunseath et al. (1997) and present better agreement with experiments for energy levels and oscillator strengths. They are logarithmically extrapolated beyond 60 eV.

The cross sections for the excitation of both multiplets by processes (1), (2) (3) and (4) are shown in Figure 1, in black for 156.1 nm and blue for 165.7 nm. Collisional cross sections from CO_2 and CO are of the same order of magnitude, while e + C is about 50 times larger than e + CO_2. They reach a maximum at lower electron energies than (1) and (2). As will be shown in the next section, despite these large differences, the much lower carbon density relative to CO_2 and CO makes electron impact on C atoms a negligible source of FUV carbon emissions.

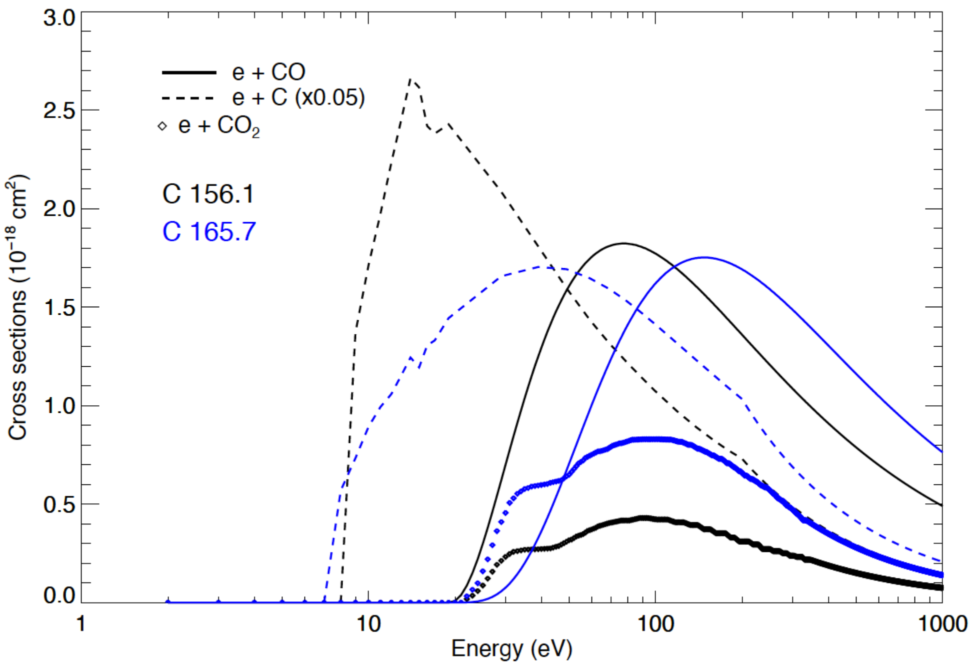

Figure 1: cross sections used to model the production of the auroral carbon emission by electron collisions on CO_2, CO and O as a function of the energy of the incident electrons. The values of the e + C cross section have been divided by 20.

2.2 Model atmosphere

For our model simulations, the vertical distribution of the CO_2, CO and O densities are given by the Mars Climate database (MCD) version 6.1 (Forget et al., 1999; Gonzalez-Galindo et al., 2013; Millour et al., 2022) previously adopted by Soret et al. (2024) to study the production of the oxygen 130.4 and 135.6 nm auroral emissions. Our reference case is for 50° south, planetary longitude of 180°, a region of strong crustal magnetic field, at midnight for southern winter solstice (L_s=90°), a region and season when bright discrete aurorae were most frequently observed and documented. Temperature and number density vertical distributions are represented in Supplementary Material Figure S1a.

Simulations for other seasons will also be discussed in the next section. The temperature and density profiles were illustrated in Figure 1 by Soret et al. (2024). The CO mixing ratio in the Martian upper atmosphere is still largely unconstrained by observations. In this study, we use the MCD profiles that are derived from the MPCM 3-D model, version 6.1. The uncertainties on the carbon monoxide abundance in the thermosphere have been discussed by Lefèvre and Krasnopolsky (2017) who pointed out the difficulties for photochemical models to produce enough carbon monoxide. For example, Gérard et al. (2023) showed that the GEM-Mars model (Neary and Daerden, 2018; Daerden et al., 2019) gives CO/CO_2 density ratios between 0.01 (L_s =120°) and 0.02 (L_s =200°), globally smaller and more constant throughout the Martian year than the MCD values. CO/CO_2 relative column abundances derived by Evans et al. (2022) from EMUS global spectral images show variability in local time, latitude, and solar longitude inconsistent with model predictions. Evans et al. (2024) analyzed EMM/EMUS limb observations of the Fourth Positive CO bands in the dayglow. They provided estimates of the mean daytime thermospheric CO density and mixing ratio during EMM orbits close to Spring equinox in the early afternoons. At 130 km, the CO mixing ratio is about twice less than in the MCD 6.1 version.

The carbon atom vertical distribution has been modeled by McElroy and McConnell (1971) and Fox and Hać (2009) and deduced from MAVEN-IUVS observations of the CI FUV dayglow by Lo et al. (2022). The latter studies give a C peak density of 4.0 x10^5 cm^{-3} at aphelion and 4.4x10^5 cm^{-3} at perihelion. However, these values all refer to daytime conditions. At night, most of the dominant carbon sources such as photodissociation of CO_2 and CO, photoelectron impact on CO and resonant scattering of solar UV photons by C atoms are shut off, while the C + O_2 loss reaction proceeds throughout the night. Consequently, these dayside model values may be considered as upper limits of the nightside density and the C density profile by Fox and Hać (2009) has been adopted in the absence of nighttime density data.

2.3 Optical thickness

Following Hubert et al. (2012) and Lo et al. (2022), we treat both transitions as optically thin since the $^3D^0$ and $^3P^0$ atoms are mainly produced by non-thermal processes (1) and (2). These exoenergic processes create fast C atoms carrying substantial kinetic energy, so that their speed exceeds by far their thermal velocity. Consequently, ambient C atoms have a low probability to resonantly scatter photons emitted by fast C atoms and the atmosphere may be considered as optically thin. The vertical brightness associated with these sources is thus the direct integration of the volume production rate along the line of sight.

For the direct electron impact on thermal carbon atoms, the optical depth τ_0 at line center is given by:

$$\tau_0 = \sigma_0 \int n_C\,(z)dl \qquad (5)$$

where σ_0 is the single scattering cross section at line center, $n_C(z)$ is the local carbon density, and the integral is made along the line of sight. Based on the oscillator strengths recommended by NIST (Kramida et al., 2020), the resonance scattering cross section at the line center of the strongest component is 2.1x10^{-13} cm^2 at 150 K for the transition at 165.69 nm, so that unit vertical optical depth is reached for an overhead column of carbon atoms of 4.8x10^{12} cm^{-2}. This vertical column density is reached near 140 km, close to the average location of the discrete auroral maximum. The values of τ_0 are different for each component of the carbon line components of the sextuplet but they all remain close to or smaller than unity. Consequently, multiple scattering may be neglected for most of the emission column. More importantly, anticipating on the Monte Carlo simulations, electron impact on C atoms is a negligible source of 165.7 and 156.1 nm auroral emission compared to the other two sources.

The absorption cross section by CO_2 at 150 K is equal to 4.7×10^{-20} cm^2 at 165.7 nm and 2.4×10^{-19} cm^2 at 156.1 nm (Venot et al., 2018). Vertical unit optical depth is reached at 68 km and 70 km respectively for the equinox conditions at 0° latitude. Absorption is therefore negligible for the discrete aurora whose emission peak typically lies near 135 km (Soret et al., 2021) but may need to be considered in some cases of diffuse SEP aurorae which peak as low as 60 km (Schneider et al., 2015, 2018) and are produced by significantly higher energy particles (Nakamura et al., 2022).

2.4 Monte Carlo calculations

Model simulations described in the next section were obtained using the Direct Simulation Monte Carlo (DSMC) method solving the Boltzmann equation to calculate the auroral electron transport equation. The model extends from 50 to 300 km and is used here to simulate monoenergetic electron precipitation. The distribution of the electron pitch angles at the top of the model is assumed to be isotropic downward over 2π steradians. It was initially developed for the Earth's atmosphere (Shematovich et al., 2008) and applied to the Mars aurora by Gérard et al. (2015, 2017), Bisikalo et al. (2017) and Soret et al. (2016, 2024), to calculate the vertical distribution of various emissions in the Mars aurora. Comparisons with the recent Monte Carlo simulation by Okiyama et al. (2025) show good agreement for electron energies up to ~35 keV. Beyond this energy, some differences appear in the peak altitude of ultraviolet emissions, possibly caused by stronger forward elastic scattering in their model. The integrated electron energy flux is taken equal to 1 mW m^{-2} throughout this study. The calculated brightness of the carbon emissions may be scaled linearly for any other value of the flux input. The evolution of the downward electron flux at 4 altitudes is shown in Supplementary Material (Figure S2). It shows similar characteristics to the earlier discussion of the penetration of the electron beam by Gérard et al. (2017) and Soret et al. (2024).

Measured auroral flux values are based on concurrent *in situ* detections of precipitating electrons and the MEx/ASPERA-2 and MAVEN/SWEA instruments. They range from 0.10 to 13.3 mW/m^2 from simultaneous ASPERA and SPICAM measurements (Gérard et al., 2015) and 1×10^{-4} to 2.7 mW/m^2 (Soret at al., 2021) based on combined SWEA and IUVS observations. The very low 1×10^{-4} mW/m^2 value was measured at 547 km and may not be correctly mapped along the magnetic field line threading the spacecraft location.

3. RESULTS OF MODEL SIMULATIONS

We first concentrate on the $2s^22p3s\ ^3P^0 \rightarrow 2s^22p^2\ ^3P$ allowed transition to the ground state, the brightest of the two FUV carbon emissions in both the dayglow and the aurora. Figure 2a illustrates the relative importance of the three sources of $C(^3P^0)$ atoms for an electron flux of 1 mW m^{-2} at the top of the model. Dissociation of CO_2 dominates the production of $C\ (^3P^0)$ atoms up to 180 km while CO dissociation becomes important at higher altitudes. Direct excitation of carbon atoms remains negligible at all altitudes because of the much lower density of C atoms. At 250 eV, a maximum production of 16 $cm^{-3}\ s^{-1}$ is predicted at 136 km, with a total vertically integrated brightness of 36 R.

Figure 2b shows the 165.7 nm production rate for a series of initial electron energies E_0 between 50 and 1000 eV. Although the precipitated energy flux remains equal to 1mW m^{-2}, the production rate increases with the electron energy, a consequence of the competition between dissociative excitation of CO_2 and other processes such as ionization, which becomes more efficient at higher electron energies. Finally, the limb integrated brightness shows a similar trend with a maximum intensity increasing from 357 R at 30 eV to 1 kR at 250 eV (panel c). As expected, the altitude of the maximum production decreases with energy, ranging from 149 km to 121 km as shown in panel (d).

$C\ (^3D^0)$ atoms giving rise to the 156.1 nm emission have similar auroral sources to the $^3P^0$ atoms but with a somewhat different energy thresholds and magnitude as shown in Figure 1. The peak altitude of the two carbon emissions remains the same for all energies beyond 30 eV (Figure S3 of the Supplementary Material). The ratio of the production of the two emissions shown in black in Figure 3 increases up to about 400 eV and stabilizes at nearly constant value of 1.5 at higher energy. This energy dependence stems from the different shapes of processes (1), (2) and (3) for the two emissions. The calculated CI 165.7 nm/CI 156.1 nm ratio varies from 0.8 to 1.6. This limited sensitivity stems from the identity of the dominant excitation process and the similar shape of the two excitation cross sections (Figure 1). The significant seasonal change between L_s=45° and 225° suggests that these line ratios depend on atmospheric composition. Better constraints on the CO density would be required to infer characteristic electron energies from the 165.7 nm/CI 156.1 nm ratio as discussed in section 4.

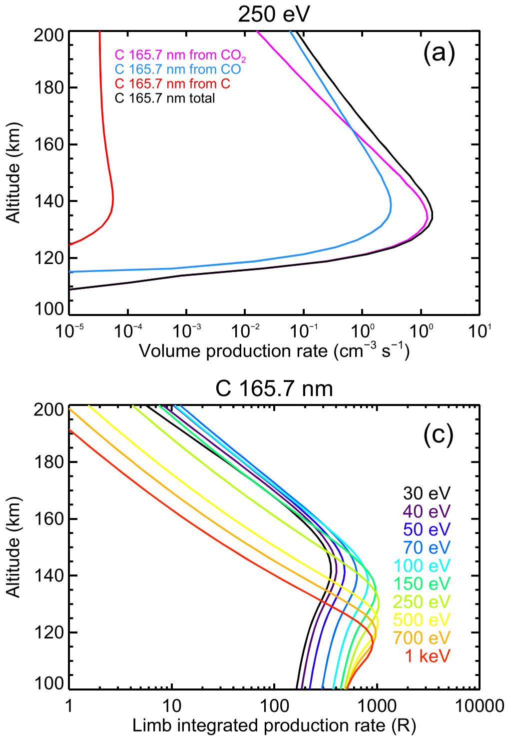

Figure 2: (a) calculated production rates of C($^3P^0$) atoms for processes (1), (2) and (3) respectively in purple, blue and red for an incident flux of 250 eV electrons carrying a flux of 1 mW m^{-2}. The total is shown in black; (b) volume production rates for electron precipitation with energies between 30 and 1000 eV; c) limb integrated production rate corresponding to (b); (d) altitude of the maximum intensity at the limb for the same initial electron energy as in (c).

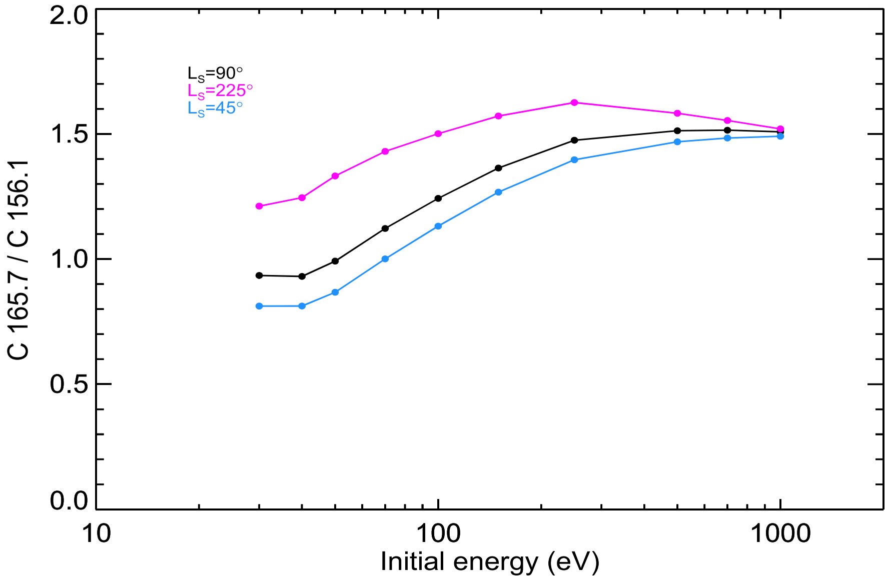

Figure 3: variation of the intensity ratio I(165.7nm)/I(156.1nm) for different initial electron energies and three seasons (latitude = 50° S, longitude=180°).

4. COMPARISON WITH OXYGEN FUV EMISSIONS AND SEASONAL VARIATIONS

Atomic oxygen emissions at 130.4 and 135.6 nm dominate the FUV Martian spectrum of the aurora, except for the SEP-induced emissions whose peak is generally located much below the discrete aurora, causing absorption of both emissions by the overlying CO_2 column. Soret et al. (2016) detected the presence of the 130.4 nm emission in SPICAM limb spectra ranging between 17 and 54 R. The EMUS Spectrometer on board the Emirates Mars Mission has provided global FUV spectral images of the Mars nightside between 110 and 180 nm. Auroral spectra and images at 130.4 nm observed with have been analyzed by Lillis et al. (2022) and Chirakkil et al. (2024). A bright auroral spectrum by Lillis et al. (2022) showed the simultaneous presence of the spin-forbidden OI 135.6 optically thin emission with a brightness ~5 times weaker than 130.4 nm.

The vertical distribution of these auroral oxygen emissions was calculated by Soret et al. (2024) using Monte Carlo electron transport calculations. It was coupled with a radiative transfer model to account for the optical thickness of the atmosphere for the OI 130.4-nm triplet. They showed that, between 30 and 1000 eV, both emissions are mainly excited by direct electron impact on ground state $O(^3P)$ atoms. They presented model calculations of the nadir ratio R1 of the two emissions for different electron energies and seasons (Figure 4, dashed lines). Their brightness strongly depends on the flux of the electrons, but their ratio is independent of the total energy flux and only weakly dependent on the O density at the auroral location. Finally, they showed that multiple scattering of the 130.4 nm photons significantly enhances the R_1= I(130.4 nm)/I(135.6 nm) nadir ratio and presented curves of the brightness ratio versus the electron energy. The dependence of the carbon line ratio R_2= (I(165.7)/I(156.1 nm) will be discussed in section 5.

A third color ratio is also expected to depend on the electron characteristic energy of the auroral electrons. For a given electron energy flux, the OI 130.4 nm nadir intensity is primarily controlled by the interaction of electrons with atomic oxygen while the brightness of the FUV carbon lines is essentially linked to CO_2 density in the region of maximum energy deposition. Therefore, when electrons penetrate deeper in the Martian atmosphere, the production of emissions from electron collisions with O decreases, while those generated by dissociation of CO_2 become more efficient. Therefore, the R_3 = I(130.4nm)/I(165.7 nm) ratio also depends on the penetration depth of auroral electrons in the Martian atmosphere. This is confirmed in Figure 4 showing this ratio in black as a function of the electron initial energy calculated for the same conditions as Figures 2a and 3. For L_s = 90°, the R_3 color ratio monotonically decreases from 50 at 30 eV to 3.8 at 1 keV and is thus dependent on the altitude of the energy of the auroral electron.

We also examined the seasonal variations of these ratios. For this purpose, we use the MCD atmospheric model to simulate the production of the OI and CI auroral emissions at other seasons. The temperature and number densities for solar longitudes L_s = 90° (equinox), 45° (winter in the southern hemisphere) and 225° (summer in the southern hemisphere) are illustrated in the Supplementary Material. Figures S3 to S7 show the equivalent of Figure 2 at

L_S= 45° and 225° for the 165.7 nm and 156.1 nm emissions. Dissociation of CO_2 remains the dominant source of excitation near the emission peak in all cases and direct excitation of C atoms is always negligible at all altitudes. The varying importance of carbon monoxide dissociation reflects the seasonal variations of the CO mixing ratio in the lower thermosphere and impact the calculated color ratios involving the CI emissions.

Figure 3 also illustrates the energy dependence of the ratio of the nadir brightness of the two carbon multiplet for L_S=225° and 45°. Although the curve for L_S=45° is close to the L_S=90° case, the values for L_S=225° are larger for all electron energies but converge to the same values at 1 keV. The nightside CO/CO_2 ratio is poorly constrained by observations and variable in this altitude range and atmospheric models show significant differences (Gérard et al., 2023, supplementary material). For example, the MCD model provides a CO/CO_2 ratio varying from 0.02 at L_s = 270° to 0.21 at L_s = 75° at 130 km, 50° S,midnight local time. In contrast, the GEM-Mars model (Neary and Daerden, 2018; Daerden et al., 2019) gives density ratios between 0.01 (L_s = 120°) and 0.02 (L_s = 200°), globally smaller and more constant throughout the Martian year than the MCD. It appears that the MCD and the GEM models show opposite seasonal dependencies of the CO abundance. As shown in Figure 3, seasonal changes of the CO mixing ratio impact the line ratio of the two carbon lines, especially at low electron energy. The present uncertainties on the CO mixing ratio somewhat limit the quantitative use of the I(165.7nm)/I(156.1nm) ratio as a proxy of the auroral electron characteristic energy. For example, at L_s= 90° for incident 250 eV electrons, the calculated nadir intensity ratio would increase from 1.5 to 1.6 if the MCD CO density is decreased by a factor of 2 and to 1.7 for a factor of 10.

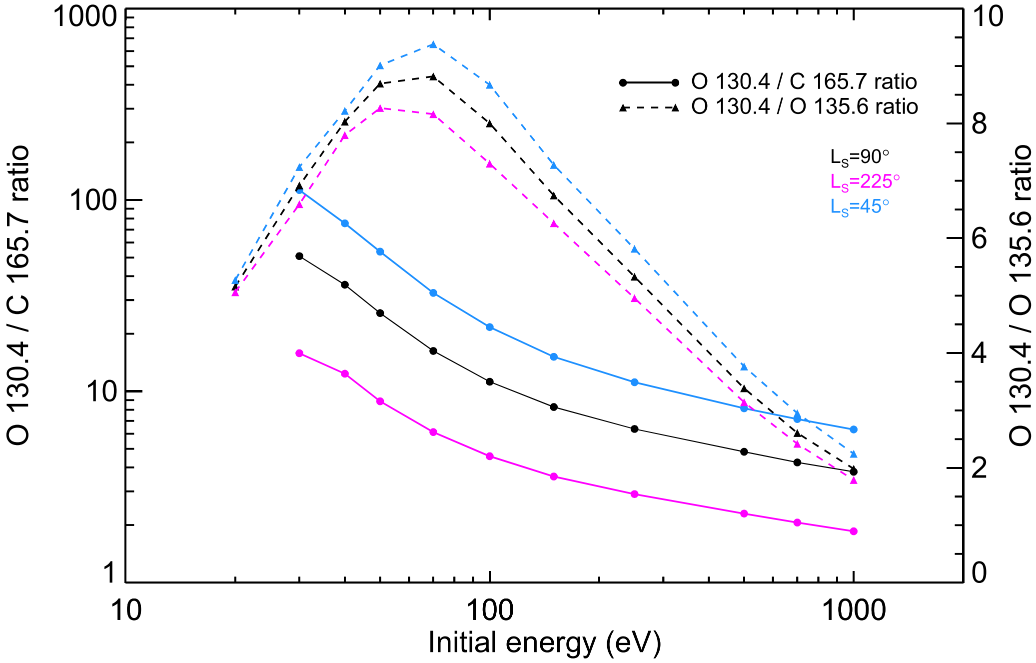

Figure 4: Solid lines: variation of the OI 130.4 nm/CI 165.7 nm nadir intensity ratio as a function of the initial electron energy for different initial electron energies for three Martian seasons (Y-axis on the left). Dashed lines: variation of the OI 130.4 nm/OI 135.6 nm nadir intensity ratio (Y-axis on the right).

5. COMPARISON WITH EMM/EMUS OBSERVATIONS

As mentioned before, the EMUS instrument (Holsclaw et al., 2021) on board the EMM-HOPE Mars orbiter has been collecting auroral FUV spectra in the wavelength range 100-170 nm. The OI 130.4 and 135.6 nm emissions are among the dominant features and occurrence maps have been presented by Lillis et al. (2022) and Chirakkil et al. (2024). In addition, the carbon multiplets at 133.5, 156.1 and 165.7 nm have been observed (Lillis et al., 2022) in the auroral spectra. For this study, a total of 3211 observations collected in 2023 were analyzed to determine the distribution of the color ratios R_1= 130.4 nm/135.6 nm, R_2= 165.7 nm/156.1 nm and R_3= 130.4 nm/165.7 nm. A range of 1.2 nm from the central wavelengths has been integrated to obtain the emission brightness of the three emissions. It includes some contribution from the Fourth Positive (4Pos) A $^1\Pi$ – X $^1\Sigma^+$ CO bands. Therefore, for the comparison with model simulations, we use Mumma et al.'s (1972) laboratory cross section for the e + CO_2 source including the energy dependent contribution of the CO 4 Pos underlying bands, presented in Figure 1. For example, the underlying (1,1) and (4,3) 4 Pos bands contribute on the order of 10% relative to the CI 156.1 nm multiplet brightness. The bandhead is at 156.0 nm and extends toward longer wavelengths so that the bands overlap the multiplet components. In the case of the 165.7 nm sextuplet, the 4Pos (0-2) band also contributes to the underlying intensity. The use of the ''effective'' energy dependent cross section is a direct way to account for this contribution, considering also that the claimed accuracy of these laboratory measurements is only 20-30%.

The dataset includes all latitudes but only pixels with solar zenith angles and phase angles larger than 120° and emission angles less than 80° are retained to avoid contamination by the dayglow limb brightening, respectively. Of these, we define "auroral" observations as those containing at least 30 pixels where 130.4 nm oxygen emission is at least 5 R. We require at least 30 pixels to ensure sufficient photon counts. This left 961 auroral observations, of which 130 had at least 30 auroral pixels in Mars' strong crustal field region (SCFR, defined as 120° to 240° East, 20° to 80° South). The resulting ratio distribution is shown in Figure 5, with the blue curves representing the SFCR. Figure 5a presents the R_1 = OI 130.4 nm/OI 135.6 nm intensity ratio. The most frequent values range between 5 and 10 (at half maximum), with a peak of 6. observations correspond to a OI 1304/OI 1356 intensity ratio exceeding the values reported in Figure 4. These high ratio values generally correspond to low 135.6 nm intensities and are thus subject to larger relative errors. They might also be caused by unusual auroral electron energy distributions, possibly corresponding to photoelectrons carried from the dayside, narrowly concentrated in the vicinity of the excitation threshold of the OI ^{5}S state giving rise to the 135.6 nm emission.

The histogram for R_2= CI 165.7 nm/CI 156.1 nm (panel b) mainly concentrates between 1 and 2 with a peak at 1.7. Finally, the R_3= OI 130.4 nm/CI 165.7 nm ratio (panel c) maximizes between 5 and 6, with half-width values between 3 and 8. The ratios observed on the strong crustal field region do not significantly depart from the global values.

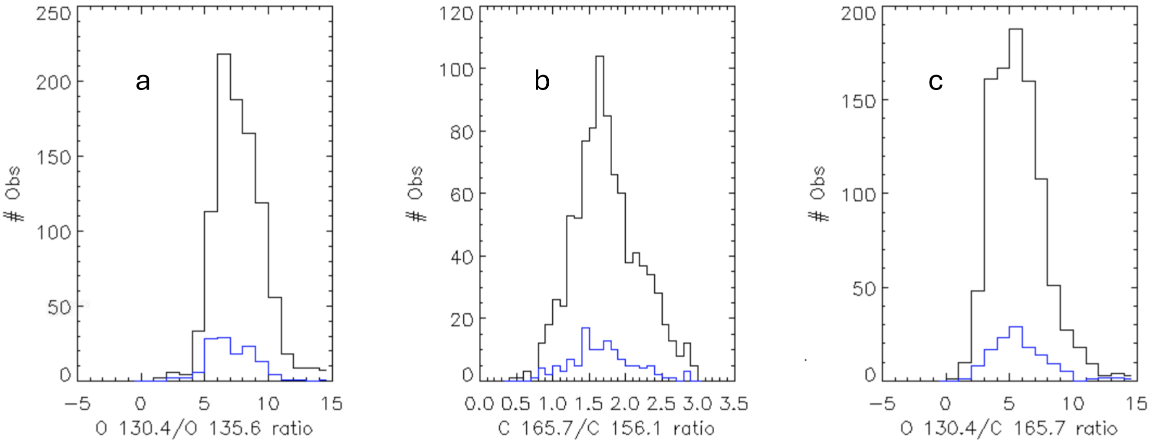

Figure 5: distribution of brightness ratios of OI and CI auroral emissions based on all EMUS nightside auroral observations collected in 2023. Black represents 961 observations with at least 30 auroral pixels, while blue represents 130 observations within Mars' strong crustal field regions (120°-240° East, 20°-80° South)

If the sets of values at half maximum from Figure 5 are combined with the curves in figures 3 and 4, the following ranges of characteristic electron energies are obtained for the L_s=90° case:

- R_1: 70 to 300 eV, with a central value of 200 eV
- R_2: 200 to 300 eV, in agreement with the calculated ratio. However, R_2 is not very dependent on electron energy. For the observed range of $1 < R_2 < 2$, the electron energy corresponds to any value above 50 eV.
- R_3: 200 eV to over 1 keV, with a central value of 300 eV.

The R_3 ratio tends to yield statical energies somewhat higher than R_1, with an overlap between 200 and 300 eV. We note that Figure 5 provides the overall statistical distribution that do not correspond to measurements of the auroral features coincident in time and space.

6. DISCUSSION

To put these results into a broader context, Figure 6 summarizes the variation of the nadir intensity of several ultraviolet and visible auroral emissions calculated for different electron energies. All simulations correspond to an incident electron energy flux of 1 mW m^{-2} and the model atmosphere described in section 2. The intensity of the two FUV carbon lines is the weakest of the group below 300 eV. Several auroral emissions (CO Cameron, OI 130.4 nm and 135.6 nm) show a decreasing production efficiency when the electron energy increases, while that of the CI multiplets , the CO_2^+ $B^2\Sigma^+ - X^2\Pi$ UV doublet and the CO_2^+ $A^2\Pi_u - X^2\Pi$) Fox-Duffendach-Barker bands (FDB) bands increases with energy. The green line and the 297.2-nm oxygen line nadir brightness show a relative flat response, with a 557.7-nm level close to 1kR. We note that the excitation cross section of the CO Cameron bands by electron impact on CO_2 is taken from Lee et al. (2022). The OI 130.4 nm curve does not include consideration of radiative transfer effects.

As mentioned before, the brightness of the CI emissions is not affected by complex radiative effects unlike the OI 130.4 nm multiplet. Their brightness is therefore a direct indicator of the precipitated electron energy flux. Figure 6 also shows their production efficiency is only moderately dependent of the initial electron energy. For a flux of 1 mW m^{-2}, the efficiency for the 165.7 nm emission is 14 R at 30 eV, 31 R at 100 eV and 29 R at 1000 eV. The production efficiencies of the CO Cameron bands in the MUV and the OI 557.7 nm (and its OI 297.2 nm proxy) are also predicted to be fairly energy independent provided that the bulk of the auroral emission remains located above the region where the parent excited states are deactivated by collisions.

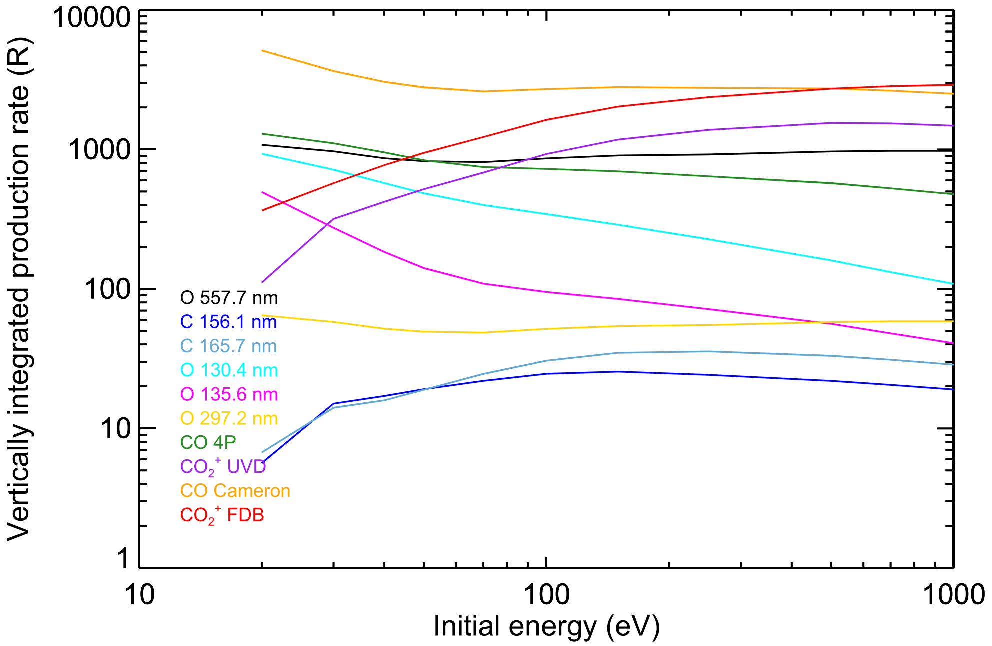

Figure 6: CALCULATED vertically integrated production rate of different auroral emissions versus the initial energy of the incident electrons for a monoenergetic precipitation of 1 mW m^{-2}. The simulations were made for a latitude of 50° S, L_s = 90° at midnight.

When compared to the EMUS intensity ratio, our simulations indicate that the Mars discrete aurora is mainly caused by electrons with initial energy less than 1 keV. This result is in full agreement with *in situ* measurements of energy spectra with the Analyzer of Space Plasmas and Energetic Atoms (ASPERA-3) and the Solar Wind Electron Analyzer (SWEA) during electron auroral precipitation. The mean energy measurement with ASPERA in conjunction with the nadir detection of a MUV discrete aurora with SPICAM ranged between 140 and 380 eV (Gérard et al., 2015). Similarly, SWEA measurements of significant energy fluxes above the aurora indicated mean energies between 66 and 216 eV (Soret et al., 2021). Xu et al. (2020) estimated to 440 eV the potential drop accelerating electrons along the magnetic field line in an inverted-V event. A statistical analysis showed that the peak energy of the electron energy distribution ranged between 50 and 150 eV (Xu et al., 2022). These values are within the range of characteristic electron energies derived from the color ratios observed with EMUS.

Future work will concentrate on EMUS mapping of the FUV color ratios and the corresponding electron energy in relation with the morphology, local time and prevailing solar wind conditions

Acknowledgements.

B. Hubert and L. Soret are Research Associates of the Belgian Fonds de la Recherche Scientifique (FNRS). L. Soret and J.-C. Gérard acknowledge support from the Belgian Federal Science Policy Office, with financial and contractual coordination by the ESA PRODEX Office. The analysis of the EMUS/EMM-HOPE observations has been supported by NASA grant 80NSSC24K1133.

Declaration of interest statement.

The authors declare that they have no known competing financial interests or personal relationships that could have appeared to influence the work reported in this paper.

Funding.

This research was partly funded by a PRODEX grant from the European Space Agency.

Data availability.

The EMM/EMUS l2a data are available at the EMM Science Data Center (SDC, https://sdc.emiratesmarsmission.ae/). This location is designated as the primary repository for all data products produced by the EMM team and is designated as long–term repository as required by the UAE Space Agency.

Appendix A. Supplementary data

Supplementary figures related to this article can be found online at https://.......
(*please indicate address to download the supplementary material.)*

CRediT authorship contribution statement.

J.-C. Gérard: Writing – original draft, Conceptualization, Investigation, Methodology Supervision, **L. Soret:** Investigation, review & editing, Visualization, Validation, Software, Methodology, **B. Hubert:** Funding acquisition, review & editing, **R. Lillis** review & editing, Investigation, Visualization, **J. Deighan:** review & editing**, S. Jain:** review & editing.

References

Ajello, J. M., Malone, C. P., Evans, J. S., Holsclaw, G. M., Hoskins, A. C., Jain, S. K., et al. (2019). UV study of the fourth positive band system of CO and OI 135.6 nm from electron impact on CO and CO_2. Journal of Geophysical Research: Space Physics, 124(4), 2954–2977. https://doi.org/10.1029/2018JA026308

Barth, C. A., Hord, C. W., Pearce, J. B., Kelly, K. K., Anderson, G. P., & Stewart, A. I. (1971). Mariner 6 and 7 ultraviolet spectrometer experiment: Upper atmosphere data. Journal of Geophysical Research, 76(10), 2213-2227, doi: 10.1029/JA076i010p02213.

Bertaux, J. L., Leblanc, F., Witasse, O., Quemerais, E., Lilensten, J., Stern, S. A., ... & Korablev, O. (2005). Discovery of an aurora on Mars. Nature, 435(7043), 790-794, DOI: 10.1038/nature03603.

Bisikalo, D. V., Shematovich, V. I., Gérard, J.-C., et al. (2017). Influence of the crustal magnetic field on the Mars aurora electron flux and UV brightness. Icarus, 282, 127-135, 10.1016/j.icarus.2016.08.035.

Chirakkil, K., Lillis, R. J., Deighan, J., Chaffin, M. S., Jain, S. K., Brain, D. A., ... & Halekas, J. S. (2024). EMM EMUS observations of FUV aurora on Mars: Dependence on magnetic topology, local time, and season. *Journal of Geophysical Research: Planets*, *129*(6), e2024JE008336, doi: 10.1029/2024JE008336.

Daerden, F., L. Neary, S. Viscardy, A. García Muñoz, R. T. Clancy, M. D. Smith, et al. (2019), Mars atmospheric chemistry simulations with the GEM-Mars general circulation model, Icarus, 326, 197-224, https://doi.org/10.1016/j.icarus.2019.02.030.

Dunseath, K. M., Fon, W. C., Burke, V. M., Reid, R. H. G., & Noble, C. J. (1997). Electron-impact excitation of the levels of carbon. *Journal of Physics B: Atomic, Molecular and Optical Physics*, *30*(2), 277, doi: 10.1088/0953-4075/30/2/020.

Evans, J. S., Correira, J., Deighan, J., Jain, S., Al Matroushi, H., Al Mazmi, H., et al. (2022). Retrieval of CO relative column abundance in the Martian thermosphere from FUV disk observations by EMM EMUS. Geophysical Research Letters, 49, e2022GL099615. https://doi.org/10.1029/2022GL099615.

Evans, J. S., Deighan, J., Jain, S., Veibell, V., Correira, J., Al Matroushi, H., ... & Yurchenko, S. N. (2024). Retrieval of Ar, N2, O, and CO in the Martian thermosphere using dayglow limb observations by EMM EMUS. *Journal of Geophysical Research: Planets*, *129*(4), e2023JE008181.

Feldman, P. D., Burgh, E. B., Durrance, S. T., & Davidsen, A. F. (2000). Far-Ultraviolet Spectroscopy of Venus and Mars at 4 Å Resolution with the Hopkins Ultraviolet Telescope on Astro-2. *The Astrophysical Journal*, *538*(1), 395, doi : 10.1086/309125.

Forget, F., Hourdin, F., Fournier, R., Hourdin, C., Talagrand, O., Collins, M., ... & Huot, J. P. (1999). Improved general circulation models of the Martian atmosphere from the surface to above 80 km. Journal of Geophysical Research: Planets, 104(E10), 24155-24175, doi: 10.1029/1999JE001025.

Fox, J. L., & Dalgarno, A. (1979). Ionization, luminosity, and heating of the upper atmosphere of Mars. J. Geophys. Res., 84(A12), 7315-7333,
doi: 10.1029/JA084iA12p07315.

Fox, J. L., & Hać, A. B. (2009). Photochemical escape of oxygen from Mars: A comparison of the exobase approximation to a Monte Carlo method. *Icarus*, *204*(2), 527-544. https://doi.org/10.1016/j.icarus.2009.07.005.

Gérard, J. C., Soret, L., Libert, L., Lundin, R., Stiepen, A., Radioti, A., & Bertaux, J. L. (2015). Concurrent observations of ultraviolet aurora and energetic electron precipitation with Mars Express. Journal of Geophysical Research: Space Physics, 120(8), 6749-6765. doi.org/10.1002/2015JA021150.

Gérard, J. C., L. Soret, V.I. Shematovich, D.V. Bisikalo, & S.W. Bougher (2017). The Mars diffuse aurora: A model of ultraviolet and visible emissions, Icarus, 288, 284–294, http://dx.doi.org/10.1016/j.icarus.2017.01.037.

Gérard, J. C., Soret, L., Hubert, B., Neary, L., & Daerden, F. (2023). The brightness of the CO Cameron bands in the Martian discrete aurora: A study based on revised cross sections. Icarus, 402, 115602. https://doi.org/10.1016/j.icarus.2023.115602.

Green, A. E. S., & Barth, C. A. (1965). Calculations of ultraviolet molecular nitrogen emissions from the aurora. *Journal of Geophysical Research*, *70*(5), 1083-1092, doi: 10.1029/JZ070i005p01083.

González-Galindo, F., J.-Y. Chaufray, M. A. López-Valverde, G. Gilli, F. Forget, F. Leblanc, R. Modolo, S. Hess, and M. Yagi (2013), Three-dimensional Martian ionosphere model: I. The photochemical ionosphere below 180 km, J. Geophys. Res. Planets, 118, 2105–2123, doi:10.1002/jgre.20150.

Holsclaw, G. M., Deighan, J., Almatroushi, H., Chaffin, M., Correira, J., Evans, J. S., et al. (2021). The Emirates Mars Ultraviolet Spectrometer (EMUS) for the EMM mission. Space Science Reviews, 217(8), 79. https://doi.org/10.1007/s11214-021-00854-3

Hubert, B., Gérard, J. C., Gustin, J., Shematovich, V. I., Bisikalo, D. V., Stewart, A. I., & Gladstone, G. R. (2010). UVIS observations of the FUV OI and CO 4P Venus dayglow during the Cassini flyby. *Icarus*, *207*(2), 549-557, doi.org/10.1016/j.icarus.2009.12.029.

Hubert, B., Gérard, J. C., Gustin, J., Bisikalo, D. V., Shematovich, V. I., & Gladstone, G. R. (2012). Cassini-UVIS observation of dayglow FUV emissions of carbon in the thermosphere of Venus. *Icarus*, *220*(2), 635-646, doi.org/10.1016/j.icarus.2012.06.002.

Itikawa, Y. (2002), Cross sections for electron collisions with carbon dioxide, J. Phys. Chem. Ref. Data, 31(3), 749– 767, doi.org/10.1063/1.1481879.

Jain, S. K., Deighan, J., Chaffin, M., Holsclaw, G., Lillis, R., Fillingim, M., ... & Eparvier, F. (2022). Morphology of extreme and far ultraviolet Martian airglow emissions observed by the EMUS instrument on board the Emirates Mars Mission. *Geophysical Research Letters*, *49*(19), e2022GL099885, doi.org/10.1029/2022GL099885.

Kramida, A., Ralchenko, Y., Reader, J., & Team, N. A. (2020). NIST Atomic spectra database (version 5.8), 2020. *National Institute of Standards and Technology: Gaithersburg, MD, USA*.

Leblanc, F., Chaufray, J. Y., Lilensten, J., Witasse, O., & Bertaux, J. L. (2006a). Martian dayglow as seen by the SPICAM UV spectrograph on Mars Express, Journal of Geophysical Research: Planets, 111(E9), doi.org/10.1029/2005JE002664.

Leblanc, F., Witasse, O., Winningham, J., Brain, D., Lilensten, J., Blelly, P. L., ... & Bertaux, J. L. (2006b). Origins of the Martian aurora observed by Spectroscopy for Investigation of Characteristics of the Atmosphere of Mars (SPICAM) on board Mars Express. *Journal of Geophysical Research: Space Physics*, *111*(A9), doi.org/10.1029/2006JA011763.

Lee, R. A., Ajello, J. M., Malone, C. P., Evans, J. S., Veibell, V., Holsclaw, G. M., ... & Schneider, N. M. (2022). Laboratory study of the Cameron bands and UV doublet in the middle ultraviolet 180–300 nm by electron impact upon CO_2 with application to Mars. *The Astrophysical Journal*, *938*(2), 99, doi :10.3847/1538-4357/ac88c8.

Lefèvre, F., & Krasnopolsky, V. (2017). Atmospheric photochemistry, in *The atmosphere and climate of Mars*, *18*, 405.

Lillis, R. J., Deighan, J., Brain, D., Fillingim, M., Jain, S., Chaffin, M., et al. (2022). First synoptic images of FUV discrete aurora and discovery of sinuous aurora at Mars by EMM EMUS. Geophysical Research Letters, 49, e2022GL099820. https://doi. org/10.1029/2022GL099820.

Lillis, R. J., Deighan, J., Chirakkil, K., Jain, S., Fillingim, M., Chaffin, M., ... & Curry, S. (2024). Sinuous aurora at Mars: A link to the tail current sheet? *Journal of Geophysical Research: Space Physics*, *129*(6), e2024JA032477.

Lo, D. Y., Yelle, R. V., Lillis, R. J., & Deighan, J. I. (2021). Carbon photochemical escape rates from the modern Mars atmosphere. *Icarus*, *360*, 114371, https://doi.org/10.1016/j.icarus.2021.114371.

Lo, D.Y., Yelle, R.V., Deighan, J.I., Jain, S.K., Evans, J.S., Stevens, M.H., Ajello, J.M., Mayyasi, M.A., and Schneider, N.M. (2022), MAVEN/IUVS observations of C I 156.1 nm and 165.7 nm dayglow: Direct detection of carbon and implication on photochemical escape, Icarus, 371, 114664, https://doi.org/10.1016/j.icarus.2021.114664.

McElroy, M. B., & McConnell, J. C. (1971). Atomic carbon in the atmospheres of Mars and Venus. *Journal of Geophysical Research*, *76*(28), 6674-6690.

Mumma, M. J., Stone, E. J., Borst, W. L., & Zipf, E. C. (1972). Dissociative excitation of vacuum ultraviolet emission features by electron impact on molecular gases. III. CO_2. The Journal of Chemical Physics, 57, 68–75, https://doi.org/10.1063/1.1678019

Millour, E., Forget, F., Spiga, A., Pierron, T., Bierjon, A., Montabone, L., ... & Cipriani, F. (2022). The Mars climate database (version 6.1). In *Europlanet science congress 2022* (Vol. 16, pp. EPSC2022-786), https://insu.hal.science/insu-04447462v1

Nakamura, Y., Terada, N., Leblanc, F., Rahmati, A., Nakagawa, H., Sakai, S., ... & Murase, K. (2022). Modeling of diffuse auroral emission at Mars: Contribution of MeV protons. *Journal of Geophysical Research: Space Physics*, *127*(1), e2021JA029914.

Neary, L., & Daerden, F. (2018). The GEM-Mars general circulation model for Mars: Description and evaluation. Icarus, 300, 458-476, https://doi.org/10.1016/j.icarus.2017.09.028.

Okiyama, T., Seki, K., Nakamura, Y., Lillis, R. J., Rahmati, A., Larson, D. E., et al. (2025). Study of variation mechanisms of the Martian diffuse aurora based on Monte Carlo simulations and MAVEN observations. Journal of Geophysical Research: Space Physics, 130, e2024JA033420, https://doi.org/10.1029/2024JA033420.

Paxton, L. J. (1985). Pioneer Venus Orbiter ultraviolet spectrometer limb observations: Analysis and interpretation of the 166-and 156-nm data. *Journal of Geophysical Research: Space Physics*, *90*(A6), 5089-5096.

Schneider, N. M., Deighan, J. I., Jain, S. K., Stiepen, A., Stewart, A. I. F., Larson, D., ... & Jakosky, B. M. (2015). Discovery of diffuse aurora on Mars. Science, 350(6261), aad0313, doi: 10.1126/science.aad031.

Schneider, N. M., Jain, S. K., Deighan, J., Nasr, C. R., Brain, D. A., Larson, D., ... & Jakosky, B. M. (2018). Global aurora on Mars during the September 2017 space weather event. *Geophysical Research Letters*, *45*(15), 7391-7398, doi.org/10.1029/2018GL077772.

Shematovich, V. I., D. V. Bisikalo, J.-C. Gérard, C. Cox, S. W. Bougher & F. Leblanc (2008), Monte Carlo model of electron transport for the calculation of Mars dayglow emissions, J. Geophys. Res., 113, E02011, doi:10.1029/2007JE002938.

Soret, L., Gérard, J. C., Libert, L., Shematovich, V. I., Bisikalo, D. V., Stiepen, A., & Bertaux, J. L. (2016). SPICAM observations and modeling of Mars aurorae. Icarus, 264, 398-406, https://doi.org/10.1016/j.icarus.2015.09.023.

Soret, L., Gérard, J. C., Schneider, N., Jain, S., Milby, Z., Ritter, B., ... & Weber, T. (2021). Discrete aurora on Mars: Spectral properties, vertical profiles, and electron energies. Journal of Geophysical Research: Space Physics, 126(10), e2021JA029495, doi.org/10.1029/2021JA029495.

Soret, L., Hubert, B., Gérard, J. C., Jain, S., Chirakkil, K., Lillis, R., & Deighan, J. (2024). Quantifying the electron energy of Mars aurorae through the oxygen emission brightness ratio at 130.4 and 135.6 nm. *Journal of Geophysical Research: Planets*, *129*(3), e2023JE008214, https://doi.org/10.1029/2023JE008214.

Venot, O., Bénilan, Y., Fray, N., Gazeau, M. C., Lefèvre, F., Es-sebbar, E., et al. (2018). VUV-absorption cross section of carbon dioxide from 150 to 800 K and applications to warm exoplanetary atmospheres. Astronomy & Astrophysics, 609, A34. https://doi.org/10.1051/0004-6361/201731295.

Wang, Y., Zatsarinny, O., & Bartschat, K. (2013). B-spline R-matrix-with-pseudostates calculations for electron-impact excitation and ionization of carbon. *Physical Review A-Atomic, Molecular, and Optical Physics*, *87*(1), 012704, doi.org/10.1103/PhysRevA.87.012704.

Xu, S., Mitchell, D. L., McFadden, J. P., Fillingim, M. O., Andersson, L., Brain, D. A., et al. (2020), Inverted-V electron acceleration events concurring with localized auroral observations at Mars by MAVEN. Geophysical Research Letters, 47, e2020GL087414, doi: 10.1029/2020GL087414.

Xu, S., Mitchell, D. L., McFadden, J.P., Fowler, C. M., Hanley, K., Weber, T., et al. (2022). Nightside auroral electrons at Mars: Upstream drivers and ionospheric impact. Journal of Geophysical Research: Space Physics, 127, e2022JA030801, doi:10.1029/2022JA030801.